

Multi-task Learning-based CSI Feedback Design in Multiple Scenarios

Xiangyi Li, Jiajia Guo, Chao-Kai Wen, *Senior Member, IEEE*,
Shi Jin, *Senior Member, IEEE*, and Shuangfeng Han, *Member, IEEE*

Abstract

For frequency division duplex systems, the essential downlink channel state information (CSI) feedback includes the links of compression, feedback, decompression and reconstruction to reduce the feedback overhead. One efficient CSI feedback method is the Auto-Encoder (AE) structure based on deep learning, yet facing problems in actual deployments, such as selecting the deployment mode when deploying in a cell with multiple complex scenarios. Rather than designing an AE network with huge complexity to deal with CSI of all scenarios, a more realistic mode is to divide the CSI dataset by region/scenario and use multiple relatively simple AE networks to handle subregions' CSI. However, both require high memory capacity for user equipment (UE) and are not suitable for low-level devices. In this paper, we propose a new user-friendly-designed framework based on the latter multi-tasking mode. Via Multi-Task Learning, our framework, Single-encoder-to-Multiple-decoders (S-to-M), designs the multiple independent AEs into a joint architecture: a shared encoder corresponds to multiple task-specific decoders. We also complete our framework with GateNet as a classifier to enable the base station autonomously select the right task-specific decoder corresponding to the subregion. Experiments on the simulating multi-scenario CSI dataset demonstrate our proposed S-to-M's advantages over the other benchmark modes, i.e. significantly reducing the model complexity and the UE's memory consumption.

Index Terms

X. Li, J. Guo, and S. Jin are with the National Mobile Communications Research Laboratory, Southeast University, Nanjing, 210096, P. R. China (email: Xiangyi_li@seu.edu.cn, jiajiaguo@seu.edu.cn, jinshi@seu.edu.cn).

C.-K. Wen is with the Institute of Communications Engineering, National Sun Yat-sen University, Kaohsiung 80424, Taiwan, and the Southern Taiwan Industry Promotion Center, National Sun Yat-sen University, Kaohsiung, Taiwan (e-mail: chaokai.wen@mail.nsysu.edu.tw).

S. Han is with the Green Communication Research Center, China Mobile Research Institute, Beijing 100053, China (e-mail: hanshuangfeng@chinamobile.com).

Massive MIMO, CSI feedback, deep learning, multitask learning, multi-scenario.

I. INTRODUCTION

A. Background

Massive multiple-input and multiple-output (MIMO) is widely regarded as one of the core technologies of the fifth-generation (5G) communication system [1] and still will be remained significant in the future 6G [2], [3]. It has the advantages of improving system capacity and spectral efficiency to ensure the transmission characteristics of "high dimension, high capacity, more dense network and lower delay" of 5G communication system [4], [5]. In massive MIMO systems, the base station (BS) must have accurate knowledge of downlink channel state information (CSI) for high-quality precoding work to guarantee a high quality and efficient transmission [5]. The downlink CSI is first acquired by user equipment (UE) and then fed back to BS in frequency-division duplexing (FDD) systems due to no reciprocity between uplink CSI and downlink CSI.

However, with the continuous growth of the number of antennas deployed at BS, the feedback becomes challenging in massive MIMO systems due to the vast CSI matrix [6]. To reduce the CSI feedback overhead, CSI should be compressed efficiently at UE before feeding back, and reconstructed at BS to recover the original high-dimensional CSI. The CSI features reflect the channel characteristics and can be regarded as a high-dimensional and low-rank image. Therefore, the mission of CSI feedback transforms into the problem of high-dimensional and low-rank image compression and reconstruction. The traditional methods, based on compressed sensing (CS) [7], are time-consuming and low efficiency, because they are iterative algorithms and hard to handle high-dimensional nonlinear problems. The CS-based methods also assume strict assumptions on channels, such as channels are sparse in some bases, which may not be satisfied in real system, leading these CS-based methods hard to deploy in practice [8].

In recent years, with the emergence of high-performance devices and massive wireless data, artificial intelligence (AI) and deep learning (DL) [9] have brought unlimited possibilities for intelligent communication [10] [11]. Especially when applying in CSI feedback, the DL-based nonlinear compression and fitting scheme has achieved great results in many works. The key idea is to utilize an end-to-end based Auto-Encoder (AE) [12] architecture, including an encoder network at UE for the dimensional reduction of the high dimensional CSI matrix and outputs the compressed code before feedbacking to BS, as well as a decoder network to reconstruct

the original CSI from the compressed code. Then, train the AE neural network (NN) offline via massive CSI samples and deploy it in the real system matching the training data. The task of CSI compression, feedback and reconstruction involves complicated, high dimensional, nonlinear and non-convex problems. Rather than the traditional CS-based methods with slow convergence rate, the DL-based data-driven methods can greatly improve the reconstruction accuracy and feedback efficiency via its excellent fitting ability towards data representation.

B. Related work

The DL-based CSI feedback framework was first introduced by CsiNet [8], which verified the great superior of NN over the traditional CS-based methods. Following it, a large amount of DL-based related works has come up to further explore the great potential of DL and focus on manifold aspects, including (1) NN architecture design: CRNet [13] designed with Multi-resolution structure; ShuffleCsiNet [14] utilized all CNN and shuffleNet to reduce NN's complexity; Work [15] adopted deep convolutional generative adversarial network (DCGAN) and perform well when the compression ratio is extremely low. (2) Quantization module optimization: CsiNet+ [16] designed the quantization module for better applying in practice and a special offset network to compensate for quantization distortion; EfficientFi [17] adopted vector quantised variational AutoEncoder (VQ-VAE) to design a trainable discrete codebook for quantization. (3) Correlation exploring: CsiNet-LSTM [18] extracted the time correlation in the time-varying channel via the recurrent NN structure; CAnet [19] designed an uplink-aided CSI acquisition framework utilizing the correlation between downlink and uplink CSI. (4) Online training: the encoder in [20] is finetuned to further improve feedback performance without changes to the decoder.

Most of the mentioned works use the dataset in [8], i.e. numerical simulation dataset in indoor and outdoor scenario generated by COST 2100 channel model [21]. To represent that NN models can be applied in practical communication systems, some AI competitions [22] [23] have held and use dataset of real system or other simulation models for participants to design sophisticated DL-based models.

C. Problem definition

In fact, the above works are all dedicating to improve the model performance, which the models are specially designed for a specific dataset. Due to the data-driven characteristic of DL,

TABLE I
NN'S PERFORMANCE VS CSI SAMPLING RANGE.

CSI Sampling range	1m	10m	40m	200m
NN's performance	-22.34dB	-5.08dB	-1.90dB	-0.77dB

* The NN tested is CsiNet [8] with compression ratio of 1/256.

* NN's performance is measured by normalized mean square error (NMSE) in dB.

NN's performance can be directly influenced by the CSI dataset, such as the sample number, the sample similarity and the feature complexity (or sparsity), which are determined by the factors of scenario's complexity or the sampling range/density. For instance, the same model CsiNet [8] has different performance on COST2100 indoor and outdoor scenario datasets due to the different scenario complexity and sampling range. Up to now, there has been no uniform standard of CSI dataset collection, and no research on how will those factors affect NN's performance, resulting in a lack of guidance and suggestions in the practical deployment, especially when facing with manifold complex scenarios.

Rather than only focusing on AE architecture design, we concentrate on bridging the gap between DL-based methods and practical deployment in this work by exploring DL's great potential from the CSI dataset's perspective. Notice that there exist a balance between the NN's performance and the sampling range, which the result on simulation dataset¹ generated by QuaDRiGa [24] software is shown in Tab I. As the sampling range expands, more scenarios are included, which increases the difference between the CSI samples, resulting in poor network performance. There are two solutions to deal with the poor performance: increase network capacity (complexity or compression ratio) or narrow CSI sampling range.

When deploying in a regular urban micro-cell with various scenarios, a NN of general complexity may not handle the CSI sampled in the whole cell with all the scenarios, but can perform well on local area with only one or a few scenarios. The challenging task of the CSI compression and reconstruction in the whole global cell can be divided into several manageable sub tasks via splitting the dataset by sampling region.

¹Each dataset includes 50,000 CSI samples, which the UE's positions are randomly sampled in a circle area with the center located 100 meters east of the BS. The sampling range is represented by the circle radius varying from 1m to 200m for comparison.

From this observation, two modes of deployment can be conducted²: (1) Design a much complicated NN to handle the global cell's CSI; (2) Divide the global cell into several local sub-areas, and use multiple relatively simple NNs, each of which is only responsible for a single local area. However, the solutions either have high computing power or memory requirements for UE, which are not suitable for low-level equipment, e.g. IoT sensor. For mode 1, a complex AE network always contains a complex encoder, requiring high computing power for UE. For mode 2, UE needs a lot of memory to store multiple sets of encoder parameters, and switch to the corresponding encoder network when it moves to another local sub-area.

D. Our contributions

In this work, we provide a new and UE-friendly designed deployment mode to address the shortcomings of mode 1 and 2. When dealing with CSI of multiple scenarios, the unmanageable overall task of the compression and reconstruction of all scenarios' CSI can be decomposed into multiple easy-tackled subtasks, i.e. compression and reconstruction of subregion's CSI. We provide this competitive multi-tasking mode of dividing the CSI dataset and feedbacking by region and propose the S-to-M (Single-encoder-to-Multiple-decoders) mode, i.e. a shared and general encoder for CSI's compression corresponds to multiple task-specific decoders for CSI's reconstruction, based on Multi-Task Learning (MTL) [25]. The shared encoder at UE can generalize to all subregion's CSI, while the task-specific decoder is special for one subregion's CSI. By adopting the hard-sharing mechanism in MTL, the shared encoder can obtain outstanding performance and generalization ability with low complexity, thus bringing a lot of convenience for UE. In addition, we add a GateNet at BS, which is trained as a classifier for the BS to choose the suitable decoder. The major contributions in this work can be summarized as follows:

- **CSI dataset segmentation:** We display the feasibility of dividing CSI dataset in multiple scenarios according to the sampling areas by analyzing the CSI feature distribution (including 1-D and 2-D feature). We also analyse the sample correlation of CSI within one subregion or across subregions, which can be regarded as a measurement of task correlation.
- **MTL applying:** To save the consumption of UE's computing power and storage capacity, we put forward a new user-friendly-designed mode, S-to-M, based on MTL. Via adopting the hard-sharing mechanism in MTL, the multiple independent AEs are jointly designed

²Assume all the NNs are trained offline before the deployment and no online adaptation or fine-tuning when deploying.

and optimized to take advantage of the task correlation. Due to MTL, the shared encoder in S-to-M's joint architecture grasps more general feature knowledge in the training, thus resulting in a strong generalization ability.

- **Autonomous switching decoder NN at BS:** In multi-tasking mode, our S-to-M uses a shared and general encoder to solve the encoder NN switching problem when the scenario changes, e.g. UE moves across subregions, while BS still faces the problem of selecting the right task-specific decoder NN. We further complete our S-to-M mode with GateNet as a classifier at BS to identify the task number from the encoder's output, enabling BS to autonomously switch decoder NN without any other additional feedback information.

We conduct the experience on dataset generated by QuaDRiGa [24] or COST2100 [21] channel model, and compare the performance and model complexity between our proposed mode and the benchmarks, which presents the advantages of S-to-M and manifests its feasibility. Moreover, simulation results show that the GateNet's supervised-learning performance (classification accuracy) of a simple NN can reach over 99.5%, bringing negligible performance loss to the original S-to-M (S-to-M without GateNet³). Finally, from the perspective of unsupervised learning, we investigate the mechanism of S-to-M mode via the compressed code's visualization and obtain an insightful understanding of the strong generalization ability of S-to-M's shared encoder.

The rest of this paper is organized as follows: Section II introduces the system model and the CSI feature analysis, which demonstrates the feasibility of dividing CSI data sets in multiple scenarios by region and lays the foundation for the subsequent multi-task modes. Section III presents the proposed MTL-based S-to-M mode for CSI feedback deployment, including the mechanism of MTL, the complete framework of S-to-M mode with GateNet and the complexity analysis. Section IV gives CSI simulation details and the evaluation of our proposed S-to-M compared with the benchmarks. The mechanism of MTL in S-to-M is further explored from the perspective of the AE's unsupervised learning, followed by the concluding marks in section V.

Notations: Vectors and matrices are denoted by boldface lower and upper case letters, respectively. $(\cdot)^H$ and $cov(\cdot)$ denote Hermitian transpose and the covariance, respectively. $\mathbb{C}^{m \times n}$ denotes the space of $m \times n$ complex-valued matrix. $[\mathbf{A}]_{i,j}$, $row_k(\mathbf{A})$ and $col_k(\mathbf{A})$ represent the $(i, j)^{th}$ element, the k^{th} row and k^{th} column in matrix \mathbf{A} . $\|\cdot\|_2$ is the Euclidean/L2 norm. $[a_k]_{k=1}^N$

³S-to-M without GateNet assumes that BS can acquire additional information, such as additional feedback information of UE's position, to identify the right subtask number.

represents a list of $[a_1, a_2, \dots, a_N]$. $para(\cdot)$ and $FLOPs(\cdot)$ denote the NN's parameter amount and the floating-point operations (FLOPs) amount.

II. SYSTEM MODEL

A. Massive MIMO-OFDM FDD System

Consider a typical urban micro-cell in FDD massive MIMO system with one BS serving for multiple single-antenna UEs. The BS is placed in the center of the cell and equipped with an N_t -antenna uniform linear array (ULA)⁴. We apply orthogonal frequency division multiplexing (OFDM) in downlink transmission over N_f subcarriers. Then the received signal on the n^{th} subcarrier for an UE can be modeled as [8]:

$$y_n = \mathbf{h}_n^H \mathbf{v}_n x_n + z_n, \quad (1)$$

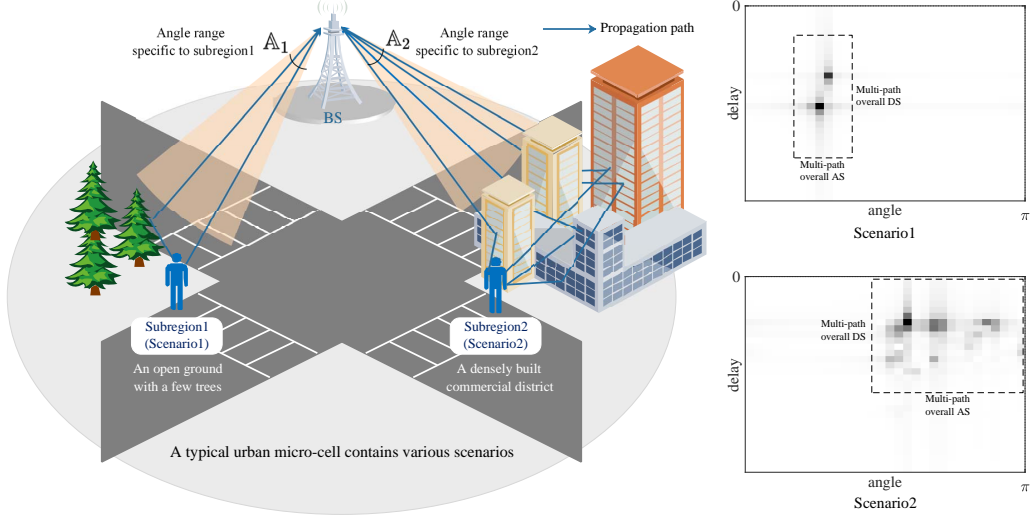
where $\mathbf{h}_n \in \mathbb{C}^{N_t}$, $x_n \in \mathbb{C}$ and $z_n \in \mathbb{C}$ denote the downlink instantaneous channel vector in the frequency domain, the transmit data symbol and the additive noise, respectively. The beamforming or precoding vector $\mathbf{v}_n \in \mathbb{C}^{N_t}$ should be designed by BS based on the received downlink CSI [26]. Stack all the N_f frequency channel vectors and we will get the downlink CSI matrix $\mathbf{H}_{S-F} = [\mathbf{h}_1, \mathbf{h}_2, \dots, \mathbf{h}_{N_f}] \in \mathbb{C}^{N_t \times N_f}$ in the spatial-frequency domain.

We conduct the same data preprocessing as in [8]: 2D discrete Fourier transformation to obtain the sparse CSI in angle-delay domain. The large dimensional CSI matrix could be sparse in angle-delay domain due to the limited multipath time delay and the sufficient antennas at BS [8]. Then we retain the first N_c ($N_c < N_f$) non-zero rows to further reduce the feedback overload and get the dimension-reduced CSI in the angle-delay domain: $\mathbf{H}_{A-D} \in \mathbb{C}^{N_t \times N_c}$. Notice that in this paper, all the grayscale images of the angle-delay CSI refers to \mathbf{H}_{A-D} . Then the complex-valued elements in \mathbf{H}_{A-D} are also divided into their real and imaginary real-valued parts, then normalized in the range of [0,1], where we finally obtain the NN's input: $\mathbf{H} \in \mathbb{R}^{N_t \times N_c \times 2}$.

B. Feature description of CSI in multiple scenarios

A typical urban micro-cell is usually contains various scenarios, each of which has its own special environmental characteristics, e.g. the distribution (density or height) of buildings, trees,

⁴We adopt the ULA model here for simpler illustration, While the analysis and the proposed model are not restrict to any specific array shape.



(a) The propagation layout between different scenarios.

(b) The grayscale map of the corresponding angle-delay CSI.

Fig. 1. A typical urban cell includes various scenarios (a), where the differences of the propagation layout can be reflected in the angle-delay CSI (b).

etc., depicting UE's surrounding scattering environment. Similar to [27], we divide the whole cell into several subregions (T subregions), in each of which users are randomly distributed and share the same (or similar) propagation environment. BS is located at an elevated position in the cell with few surrounding scatterers [28], thus the channel between BS and UE is much more affected by UE's surrounding scatterers than BS's, as depicted in Fig1(a).

Then, for the u^{th} UE, we can get the multi-path frequency response channel vector \mathbf{h}_n on the n^{th} subcarrier in equation1 according to the clustered response model⁵ [29]:

$$\mathbf{h}_n = \sum_{\ell=1}^L \iint_{\tau_{\ell} \in \mathcal{T}_{\ell}, \phi_{\ell} \in \mathcal{A}_{\ell}} |\alpha_{\ell}| e^{j\theta_{\ell} - j2\pi f_n \tau_{\ell}} \mathbf{a}_t^H(\phi_{\ell}) d\phi_{\ell} d\tau_{\ell} \quad (2)$$

where L and f_n denote the propagation path number and the n^{th} subcarrier frequency with $|\alpha_{\ell}|$, θ_{ℓ} , τ_{ℓ} , ϕ_{ℓ} , \mathcal{T}_{ℓ} and \mathcal{A}_{ℓ} stand for real-valued attenuation amplitude, the random phase shift, the delay, the azimuth angles of departure (AoDs), the delay's range and the AoD's range associated

⁵The CSI dataset for all the experiments in this paper is simulated by QuaDRiGa [24] and COST2100 [21], both of which belong to the geometry-based stochastic channel models (GSCMs), described by the clustered response model.

with the ℓ^{th} path, respectively. $\mathbf{a}_t(\phi_\ell)$ stands for the antenna array response vectors at BS, and the ULA antenna array response vectors can be given as [27] [28] [30]:

$$\mathbf{a}_t(\phi_\ell) = \frac{1}{N_t} [1, e^{-j\varpi_n \sin(\phi_\ell)}, \dots, e^{-j\varpi_n(N_t-1) \sin(\phi_\ell)}]^T \quad (3)$$

in which $\varpi_n = 2\pi df_n/c$ with c and d denoting the speed of light and the distance between antenna elements, respectively.

Following the above Eq2-3, the channel fading effects, such as the multi-path or the spatial scattering, are captured in the CSI matrix, and the multi-path propagation can be resolved in the angle-delay domain. In the clustered channel model, channels are expected to have limited L scattering and each cluster contributes a single main propagation path (resented by several sub-paths) between the BS and UE [31] [32], resulting in a small angular spread (AS) or delay spread (DS) of each path in the antenna or bandwidth resolution space [24].

For the u^{th} UE's ℓ^{th} propagation path, the AoD's range is given as $\mathcal{A}_\ell \triangleq [\bar{\phi}_\ell - \Delta_{\phi,\ell}, \bar{\phi}_\ell + \Delta_{\phi,\ell}]$ with $\bar{\phi}_\ell$ and $\Delta_{\phi,\ell}$ denoting the mean ϕ_ℓ and the AS of the ℓ^{th} path, as well as the delay's range: $\mathcal{T}_\ell \triangleq [\bar{\tau}_\ell - \Delta_{\tau,\ell}, \bar{\tau}_\ell + \Delta_{\tau,\ell}]$ with $\bar{\tau}_\ell$ and $\Delta_{\tau,\ell}$ denoting the mean τ_ℓ and the DS. This can be observed in Fig1, where 1(a) depicts two different scenarios and the propagation layout, as well as 1(b) shows the corresponding CSI's grayscale map simulated by QuaDRiGa. Especially for UE in scenario1 (an open ground), the propagation layout only contains a Line of Sight (LOS) path and an Non-LOS (NLOS) path, reflecting in the CSI map with the positions of the feature spots manifest the different path lengths and AoDs between LOS and NLOS, and the range of spots represent AS and DS [30].

Moreover, for the u^{th} UE, the overall multi-path angle range and delay range in Fig1(b) can be expressed as: $\mathcal{A}_u \triangleq \bigcup_{\ell=1}^L \mathcal{A}_{u,\ell}$ and $\mathcal{T}_u \triangleq \bigcup_{\ell=1}^L \mathcal{T}_{u,\ell}$, respectively, with $\mathcal{A}_{u,\ell}$ and $\mathcal{T}_{u,\ell}$ specific to the ℓ^{th} path of the u^{th} UE. As depicted in Fig1(a), \mathcal{A}_u and \mathcal{T}_u can be covered by (or limited to) an angle range and a delay range upper bound specific to the subregion where UE resides, respectively, i.e. $\mathbb{A}_k \triangleq \bigcup_{u \in U_k} \mathcal{A}_u$ and $\mathbb{T}_k \triangleq \bigcup_{u \in U_k} \mathcal{T}_u$ with U_k denoting the index set of UE within the k^{th} subregion.

This statistical distribution phenomenon can be also viewed in Fig2, where the multi-scenarios CSI samples in 5 subregions are simulated by QuaDRiGa [24] with more details in CharIV-A1. More specifically, each row contains 6 CSI samples randomly sampled in the corresponding subregion. In each CSI map, x axis and y axis correspond to the angle and delay domain, respectively, and the power delay profile (PDP) and power angular spectrum(PAS) are also

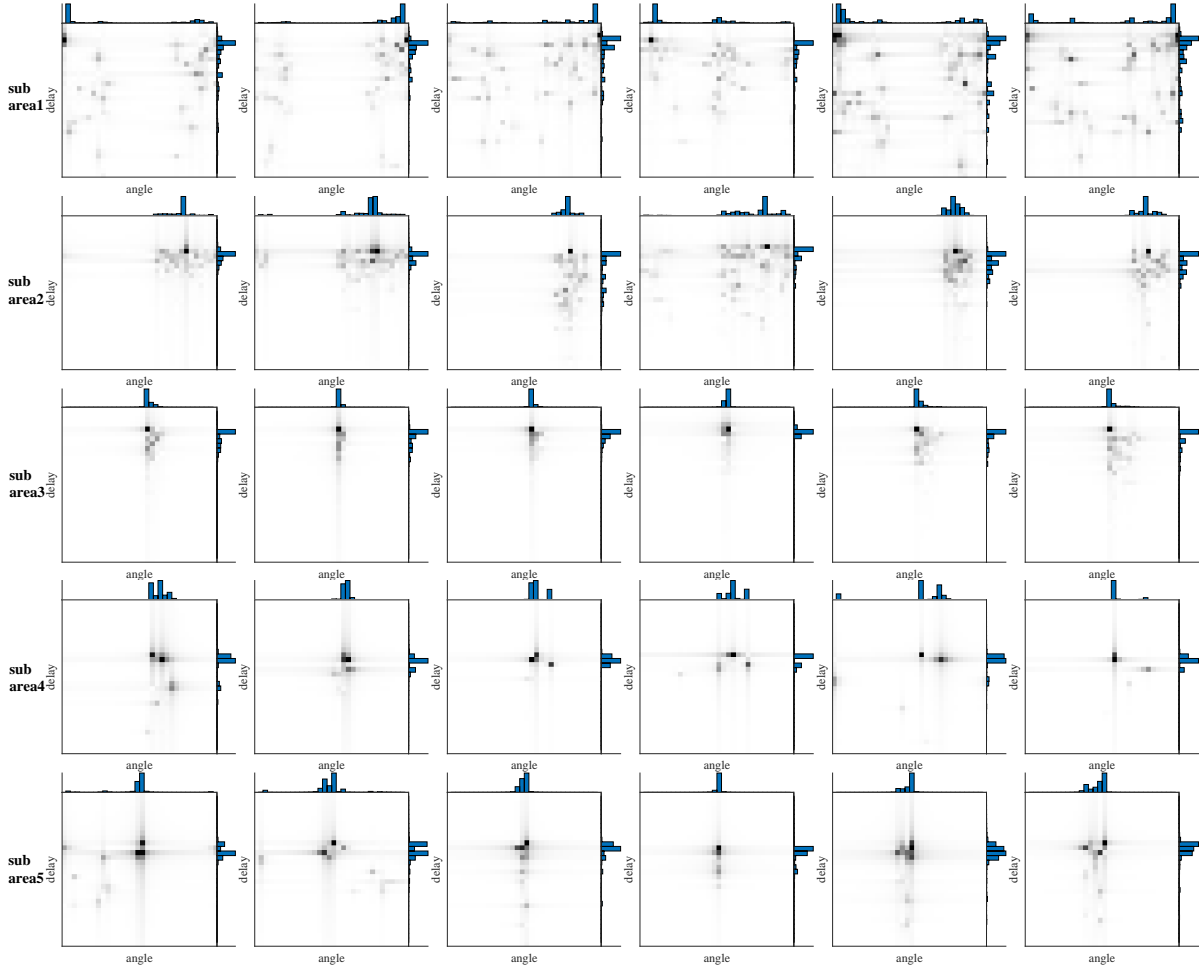


Fig. 2. Grayscale image & PAS distribution & PDP distribution of CSI maps in 5 subregions (subtasks).

depicted on the right and above the CSI image, represented the 1-D feature distributions, which can be calculated according to Eq2-3 as:

$$\begin{aligned}
 PAS(\mathbf{H}) &= \frac{1}{N_t} \left[\|col_k(\mathbf{H})\|_2^2 \right]_{k=1}^{N_t} \\
 PDP(\mathbf{H}) &= \frac{1}{N_c} \left[\|row_k(\mathbf{H})\|_2^2 \right]_{k=1}^{N_c}
 \end{aligned} \quad (4)$$

where \mathbf{H} , $\|\cdot\|_2$, $col_k(\cdot)$ and $row_k(\cdot)$ denote the CSI matrix, the Euclidean norm, the k^{th} column and row of matrix, respectively. One can observe that in each row (subregion), the 1-D and 2-D CSI features are distributed over a large or small range/image area, determined by the environmental characteristics of the corresponding subregion.

The CSI feature depicts its spacial scattering environment via the feature of AoD and path delay distribution because the propagation path can be much affected by the spatial distribution of

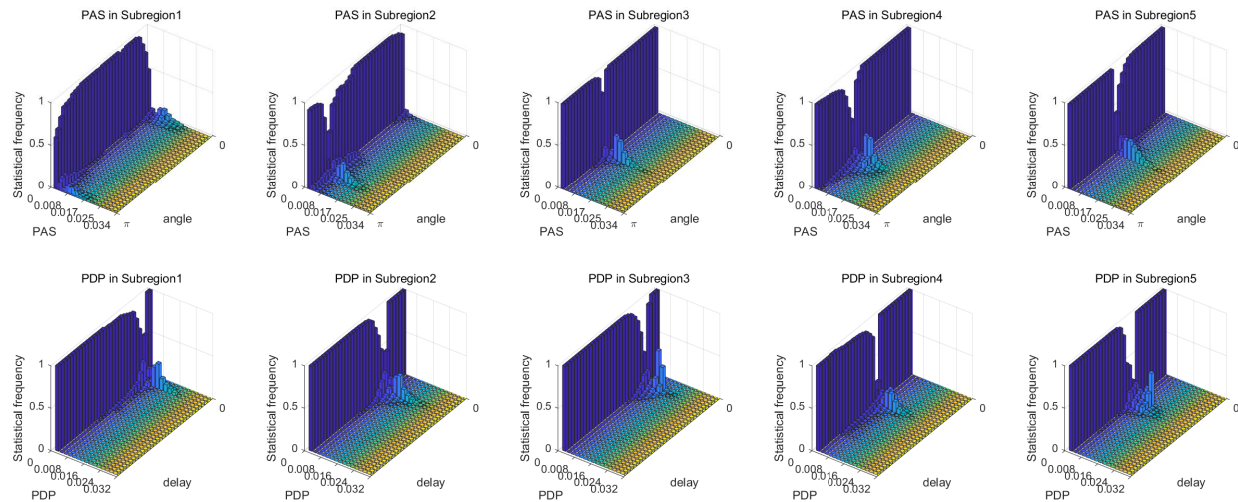


Fig. 3. Statistical frequency distribution histogram of the 1-D feature (PAS and PDP) for CSI samples.

the scatters around the UE. Thus the scenario-oriented CSI feature distribution should be closely related to the UE’s surrounding environmental properties, e.g. the shape of the scattering areas and spatial density of the scatterers. For instance, a rich scattering environment, e.g. commercial district (subarea1 in Fig2), would be reflected in a dense and complex CSI with a wide angular range and delay range, while the CSI map of an open scattering environment (Park/subarea3 in Fig2) would be sparse, which the feature is centrally distributed.

C. Subtask correlation analysis

Subsection II-B described that the CSI features are much related to the UE’s surrounding scattering environment, making it reasonable to split the dataset by the sampling region, and lays the foundation for the multitasking modes, i.e. multiple subtasks for the feedback of subregion’s CSI. These subtasks are isomorphic, which the only difference is laid in the CSI dataset. In this subsection, we focus on exploring the correlation of subtasks via analysing the statistical properties of the multi-scenario’s CSI dataset, e.g. sample’s statistical frequency and similarity, which is also the basis for the applying of MTL in our S-to-M mode.

Fig2 gives a straightforward sense of the differences in the 1-D feature (PAS/PDP) distribution of multi-scenario’s CSI via displaying several samples’ visualization. To further demonstrate, we give the statistical frequency distribution histogram of the 1-D feature for CSI in Fig3, where PAS in the first row and PDP in the second row, and each column represents

one subregion. For each subregion, the statistical frequency analysis is based on 50,000 CSI samples randomly sampled in the local subregion, which is sufficient to represent the overall CSI feature distribution of the subregion. Denote \mathbb{D}_k as the dataset of the subtask \mathcal{S}_k for the k^{th} subregion's CSI feedback. The sample statistical frequency distribution of \mathbb{D}_k is presented by its probability density function (PDF), $p_{a,k}(PAS, \phi)$ or $p_{d,k}(PDP, \tau)$ ⁶, which can be regarded as an approximate representation of the overall feature distribution, i.e. $\mathcal{D}_k \triangleq \{\mathbf{H} | PAS(\mathbf{H}) \sim p_{a,k}(PAS, \phi) || PDP(\mathbf{H}) \sim p_{d,k}(PDP, \tau)\}$.

Moreover, the CSI maps sampled within a local area have higher correlations than those sampled crossing different local areas which explains why the performance of NN in local sub areas is better than that of the whole cell from the perspective of sample similarity. More specifically, we restrict the range of these local sub-areas, represented by diameter, to less than the correlation distance, so that the large-scale fading parameters (LSPs) within one local area do not change considerably and keep their wide-sense stationary (WSS) properties [24]. Therefore, the change of small-scale fading parameters (SSPs) is the main factor affecting the difference of CSI distribution in the local sub-area, while both the LSPs and SSPs change dramatically crossing different sub-areas, resulting in a much lower CSI correlation.

Therefore, it is reasonable to divide the dataset according to the sampling area, which is equivalent to an artificial sample clustering process. Pearson correlation is introduced here to describe the similarity between CSI samples and the $(i, j)^{th}$ element in correlation matrix \mathbf{R} can be expressed as:

$$\mathbf{R}[i, j] = \frac{cov(\mathbf{H}_i, \mathbf{H}_j)}{\sqrt{cov(\mathbf{H}_i, \mathbf{H}_i)cov(\mathbf{H}_j, \mathbf{H}_j)}} \quad (5)$$

where $cov(\cdot)$ denotes the covariance. The 1-D feature distribution, i.e. distribution of power angular spectrum (PAS) and power delay profile (PDP), are given as:

$$\begin{aligned} PAS(\mathbf{H}) &= [||col_k(\mathbf{H})||_2]_{k=1}^{N_t} \\ PDP(\mathbf{H}) &= [||row_k(\mathbf{H})||_2]_{k=1}^{N_c} \end{aligned} \quad (6)$$

In Fig4, the left and middle correlation matrix are calculated via substituting $PDP(\mathbf{H})$ in equ5 for vectors $PAS(\mathbf{H})$ and $PDP(\mathbf{H})$, revealing that these two 1-D feature distribution can also

⁶The PDF of 1-D feature can be viewed as the marginal PDF of 2-D feature. We only display the marginal PDF for the convenience of visualization.

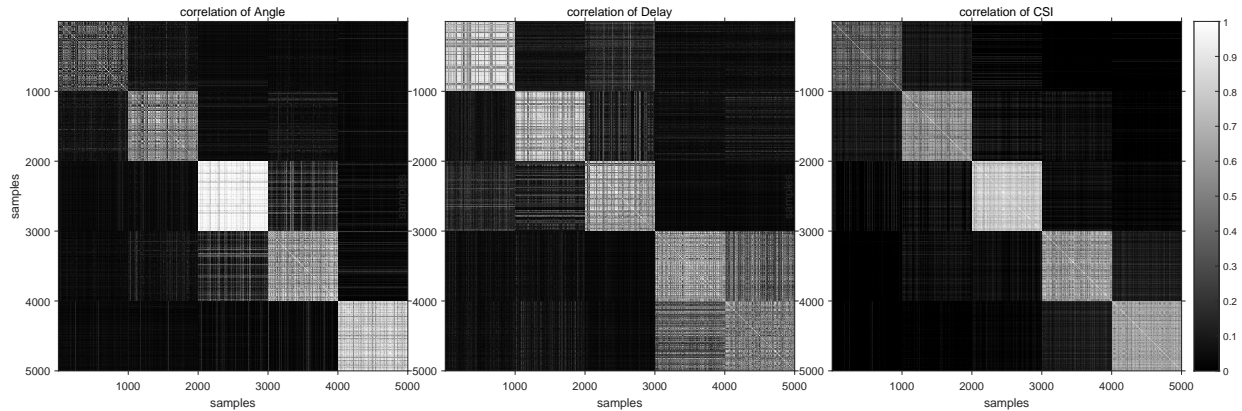


Fig. 4. Visualizes the sample correlation(Pearson correlation) matrix given the 5000 CSI samples, which are randomly sampled in 5 different local areas and each one includes 1000 samples. Left: correlation of power-angular spectrum; middle: correlation of power delay profile; right: correlation of CSI matrix. More scenario details are shown in sectionIV-A1. The small square matrix on the diagonal are shallower than the rest, manifesting that the Pearson correlation of CSI samples within a local area is higher than those crossing different areas.

maintain this correlation property, that the CSI samples of a sub-task (within a local sub-area) have higher similarity, making sub-tasks easier to fit.

III. MTL-BASED CSI FEEDBACK

In this section, the key idea and the detailed S-to-M mode of the MTL-based CSI feedback framework are described.

A. Benchmarks of deployment mode

In sectionII, we analyze the CSI feature distribution and describe that it is feasible to decompose a problematic task into multiple relatively easy sub-tasks by dividing CSI datasets according to sampling areas. Therefore, when dealing with CSI sampled from the whole cell with multiple scenarios, two deployment modes are usually adopted:

- S-to-S (single encoder to single decoder) mode (Fig 5(a)): devoting to design a single sophisticated NN with high complexity to manage the whole cell's CSI feedback.
- M-to-M (multiple encoders to multiple decoders) mode (Fig 5(b)): dividing the CSI dataset and feedbacking by region, i.e. using multiple relatively simple NNs, each is responsible for the feedback of CSI sampled in the local sub-area.

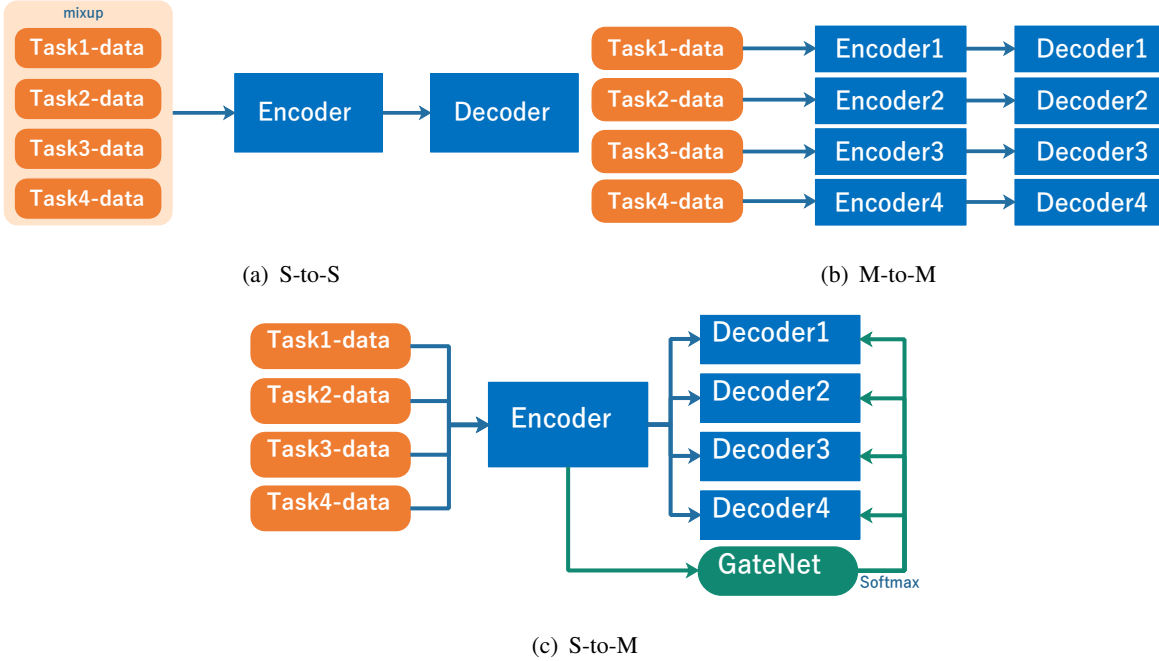


Fig. 5. S-to-S/M-to-M/S-to-M modes of deployment, where the number of sub-tasks is 4 as an example.

Obviously, the S-to-S mode is not suitable for users of low-end devices. For example, the hundreds of megabytes encoder network model designed in AI competition [22] may not be deployed in low-end devices such as small sensors in practice. Meanwhile, M-to-M mode is also not friendly enough for low-end UE. Although M-to-M mode greatly reduces the complexity of NN, especially the encoder NN at UE, and saves a lot of resource cost in NN architecture designs and parameter adjustment, it increases the link of switching network according to environment and area in actual deployment. When the UE travels from one sub-area to another, both the current encoder NN and decoder NN are not suitable for the dramatically changed CSI due to the limited generalization ability, and need to alter to the corresponding NN. Moreover, M-to-M mode needs UE to be equipped with large memory to save multiple sets of encoder NN's parameters, which brings a great burden to the UE.

B. MTL-based deployment mode

a) *Motivations:* The motivations of our proposed S-to-M deployment mode come from two aspects. On one hand, although the M-to-M mode finds a balance between the model complexity and the CSI sampling range, it does not fully take advantage of MTL, that the multiple NNs are designed independently. In this case, there is a non-negligible task correlation between multiple

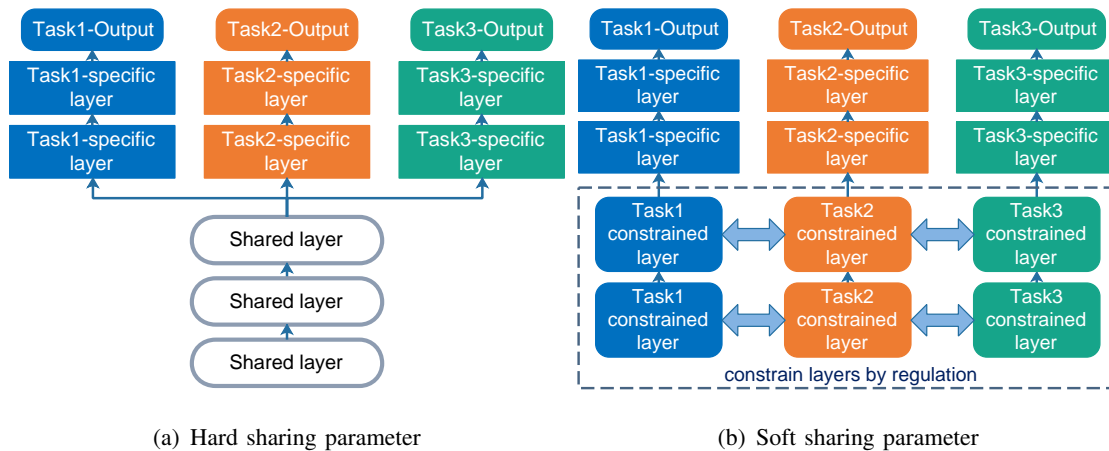


Fig. 6. Hard-sharing and soft-sharing mechanisms in MTL, where different tasks are colored differently.

tasks. The feature distribution of CSI sampled in different sub-areas will be affected by some common factors, such as the number and distribution of BS antennas, the climate of the whole cell, the performance of transceiver equipment, etc. Therefore, we introduce MTL to improve the M-to-M mode via jointly designing the multiple NNs to explore this task correlation and learn the sharing representations.

On the other hand, the S-to-S or M-to-M modes require high computational power or memory of UE. So, does a framework exist that can maintain the same simple network complexity as M-to-M mode and deploy a general encoder with strong generalization ability in UE as the S-to-S mode? Inspired by this, we design a new MTL-based CSI Feedback deployment mode, S-to-M, via utilizing the hard-sharing structure of MTL, where a common and shared encoder corresponds to multiple task-specific decoders, depicted in Fig5(c). With the help of exploring the task correlation via MTL, the shared encoder can obtain outstanding performance and generalization ability with low complexity.

b) MTL applying: MTL is a relatively mature technology in machine learning, and has made good achievements in many fields. The basic idea of MTL is to combine multiple relative tasks to learn at the same time to enhance each model's representation and generalization abilities, which is mainly realized by sharing representations between related tasks through the mechanism of sharing parameters [33]. The main parameters sharing mechanism of deep MTL are two kinds depicted in Fig6: (1) Hard-sharing (Fig6(a)) architecture stacks the task-specific layers on the top of the shallower shared layers [34]; (2) Soft-sharing (Fig6(b)) approaches allow each task

has its own parameters and model, where the distance between model parameters is regularized to encourage parameter similarity [35].

Here, we choose the hard-sharing architecture to design our MTL-based CSI feedback mode, as it is not only more suitable for closely related tasks, but also more appropriate for our UE-friendly-design needs. Moreover, the hard parameter sharing greatly reduces the overfitting risk of the shared parameters (specifically reduces to $1/T$ of the unshared parameter's, where T is the number of sub-tasks [36]). An intuitive understanding is that the shared parameters can access to the samples from all tasks whereas the task-specific parameters only access to its own sub-task samples, thus enabling the shared part hard to find a representation that captures all of the tasks, i.e. hard to have an overfitting problem. It is equivalent to a kind of data enhancement, assisting the shared parameters to obtain the outstanding performance and generalization ability with low complexity.

In our S-to-M mode, the shared encoder is designed as the sharing parameter part in the hard-sharing architecture to extract the sharing representation and exploit the task correlation, such as the factors of transceiver equipment's performance or the consistency of geography and climate in the whole cell. Meanwhile, the multiple decoders stand for the top task-specific layers to learn the differences between the sub-tasks, e.g. LSPs and SSPs. Given T sub-tasks, the outputs of the three mentioned modes can be expressed as:

$$\begin{aligned}
 S - to - S : \quad \hat{\mathbf{H}}_k &= Dec(Enc(\mathbf{H}_k, \Phi), \Psi) \\
 M - to - M : \quad \hat{\mathbf{H}}_k &= Dec_k(Enc_k(\mathbf{H}_k, \Phi_k), \Psi_k) \\
 S - to - M : \quad \hat{\mathbf{H}}_k &= Dec_k(Enc(\mathbf{H}_k, \Phi), \Psi_k)
 \end{aligned} \tag{7}$$

, where $k \in \{1, 2, \dots, T\}$ means the index of the sub-task. \mathbf{H}_k and $\hat{\mathbf{H}}_k$ are the input and output corresponded to the k^{th} sub-task, respectively. $Enc(\Phi)$ and $Dec(\Psi)$ stand for the shared and common encoder and decoder, while $Enc_k(\Phi_k)$ and $Dec_k(\Psi_k)$ are correspond to the k^{th} sub-task.

C. Framework of S-to-M mode with GateNet

a) *Framework Architecture*: Notice that the MTL-based CSI feedback mode involves the problem of switching the decoder networks when UE moving across different sub-areas, that some extra environmental information should be feedback to the BS for guiding work, such as UE's position. To further improve and complete the S-to-M deployment mode framework, we

add a classifier NN, GateNet, at BS to output the label from the encoder's output and conduct BS to switch for the correct decoder networks. In this way, no more extra information are involved to increase the feedback overhead, which also simplifies the process of CSI feedback in multiple sub-areas.

The overall framework of S-to-M mode with GateNet is depicted in Fig5(c), where the encoder at UE is equipped with one shared encoder NN, while the decoder at BS is equipped with multiple task-specific decoder NNs (colored in blue). A simple classifier GateNet is also deployed at BS (colored in green) to identify the task category to which the CSI sample belongs through the compressed feedback code. GateNet consists with three fully-connected (FC) layers, whose the output length are 2048/512/T. The output of GateNet is given as:

$$\mathbf{g} = \sigma(\mathbf{W}_3(\mathbf{W}_2(\mathbf{W}_1 \cdot \mathbf{s} + \mathbf{b}_1) + \mathbf{b}_2) + \mathbf{b}_3) \quad (8)$$

where $\mathbf{s} = Enc(\mathbf{H}, \Phi)$ is the shared encoder's output; \mathbf{W}_i and \mathbf{b}_i ($i = 1, 2, 3$) mean the weight matrix and the bias of the three FC layers; σ is the softmax activity to output the the most likely category in the form of maximum probability. We can also convert g to the sub-task index identified by GateNet via $g = argmax(\mathbf{g})$. When being deploying, the BS first lets the GateNet to identify the sub-task index once it receives the feedback code, then picks the corresponded decoder for CSI decompression and reconstruction. Therefore, given a k^{th} sub-task's CSI sample \mathbf{H}_k , the output of the overall S-to-M mode with GateNet is expressed as:

$$\hat{\mathbf{H}}_k = Dec_g(Enc(\mathbf{H}_k, \Phi), \Psi_g) \\ where \quad g = argmax(GateNet(Enc(\mathbf{H}_k, \Phi))) \quad (9)$$

Although the expression shows that this overall MTL-based CSI feedback framework is much affected by the GateNet's classification accuracy, the nearly perfect performance (accuracy over 99.9%) in the experimental results manifest that the loss brought by GateNet is small enough to be ignored. The encoder's output contains adequate information for GateNet's classification work.

b) Training: The training of the overall framework can be divided into two steps: First, train the S-to-M architecture (colored blue in Fig5(c)), i.e. jointly train the shared encoder and

multiple decoders with the joint loss function:

$$\begin{aligned} L_{S-to-M} &= \frac{1}{T} \sum_{k=1}^T L_{MSE}^{(k)} \\ &= \frac{1}{T} \frac{1}{N} \sum_{k=1}^T \sum_{n=1}^N \left\| \hat{\mathbf{H}}_k^{(n)} - \mathbf{H}_k^{(n)} \right\|_2^2 \end{aligned} \quad (10)$$

where N and T denote the batch size and the number of sub-tasks; $\hat{\mathbf{H}}_k^{(n)} = Dec_k(Enc(\mathbf{H}_k^{(n)}, \Phi), \Psi_k)$ is the reconstruction of an CSI sample $\mathbf{H}_k^{(n)}$ from the k^{th} sub-task dataset.

Second, train the GateNet (colored green in Fig5(c)): fix the S-to-M's parameters Φ to obtain the encoder's output $\mathbf{s}_{k,n} = Enc(\mathbf{H}_k^{(n)}, \Phi)$, label them with the corresponding task category with one-hot code $\ell_{k,n} = \ell_k$, where the i^{th} element: $\ell_k[i] = \begin{cases} 1 & \text{if } i=k \\ 0 & \text{else} \end{cases}$. Then we get the training data $\bigcup_{k=1}^T \{(\mathbf{s}_{k,n}, \ell_{k,n})\}_{n=1}^{N_k}$ (N_k is the number of dataset samples for the k^{th} sub-task) of the classifier GateNet for supervised learning. A basic classification loss function, cross entropy, is utilized to train GateNet:

$$L_{GateNet} = \frac{1}{N} \sum_{n=1}^N \sum_{i=1}^T \ell_{k,n}[i] \log(\mathbf{g}_{k,n}[i]) \quad (11)$$

where $\mathbf{g}_{k,n} = GateNet(\mathbf{s}_{k,n})$ and $\mathbf{g}_{k,n}[i]$ denotes its i^{th} element. N samples are randomly captured from $\bigcup_{k=1}^T \{(\mathbf{s}_{k,n}, \ell_{k,n})\}_{n=1}^{N_k}$ for batch training.

c) Complexity analysis: Considering that the S-to-M mode can adopt NN with any architecture or complexity, we mainly discuss and compare the complexity between our purposed S-to-M mode and the S-to-S or M-to-M modes. For convenience, the multiple task-specific decoder NN architectures are the same in the analysis, yet the S-to-M mode is not restricted to this limitation. To be fair, the comparison is under the situation that the three modes obtain the same leveled performances and feedback overhead, where the S-to-S mode would apply a much more complicated encoder and decoder NN, denoted as Enc_{com} and Dec_{com} (combination denoted as AE_{com}), while the encoder and decoder NN in the mode with multiple NN (M-to-M or S-to-M) would be more simple and light-weighted, denoted as Enc_{sim} and Dec_{sim} (combination denoted as AE_{sim}). Table II gives the comparison of memory consumption, offline training and online inference time consumption, where the memory consumption and time consumption are proportional to space and time complexity, respectively, i.e. parameter and computational amount (FLOPs).

TABLE II

COMPARISON OF MEMORY CONSUMPTION, OFFLINE TRAINING AND ONLINE INFERENCE TIME CONSUMPTION BETWEEN S-TO-S/M-TO-M/S-TO-M.

Mode	S-to-S	M-to-M	S-to-M + GateNet
Enc Memory	$para(Enc_{com})$	$T \cdot para(Enc_{sim})^1$	$para(Enc_{sim})$
Dec Memory	$para(Dec_{com})$	$T \cdot para(Dec_{sim})$	$T \cdot para(Dec_{sim}) + para(GateNet)$
Offline training time ²	$TN \cdot O(FLOPs(AE_{com}))$	$TN \cdot O(FLOPs(AE_{sim}))$	$TN \cdot [O(FLOPs(AE_{sim})) + O(FLOPs(GateNet))]$
Online Inference time	$O(FLOPs(AE_{com}))$	$O(FLOPs(AE_{sim}))$	$O(FLOPs(AE_{sim})) + O(FLOPs(GateNet))$

¹ T and N denote the tasks number and the training samples number in every sub-task, respectively.

² In S-to-S mode, there is one NN trained with $T \cdot N$ samples, while in M-to-M mode, there are T small NNs, each trained with N samples.

In Table II, T , N and $O(\cdot)$ stand for the tasks number, the training samples number and the infinitesimal of the same order, respectively. When comparing S-to-S with the multitasking modes, the subsequent experiment results show that both the parameters and FLOPs amount of AE_{com} are much larger than AE_{sim} , even larger than $T \cdot para(AE_{sim})$ or $T \cdot FLOPs(AE_{sim})$, reflecting the feasibility and advantages of M-to-M or S-to-M mode in terms of complexity, whose the memory and time consumption are less than the S-to-S mode. We then compare our proposed S-to-M mode with the M-to-M mode. As an upgraded version of M-to-M, S-to-M only save one set of encoder’s parameters, reducing much memory consumption at UE. In the remaining indicators, S-to-M increases the complexity brought by the GateNet compared with M-to-M, but because GateNet is a very small network composed of only three FC layers, this increased complexity can be ignored. Moreover, GateNet also eliminates the need for UE to feed back additional information to BS in real time to switch network parameters.

Due to the S-to-M’s structure of multiple paralleled decoders and the jointly training process, the only defect is that it may occupy a large amount of graphics memory during training when the sub-task number grows too large. However, it is not tricky for BS with high-performance equipment, and this problem can be solved by parallel or distributed training with multiple GPUs.

IV. SIMULATION RESULTS AND DISCUSSIONS

In this section, we first provide the details in CSI dataset simulation and NN training. Then, we evaluate and compare the proposed MTL-based CSI feedback deployment mode, S-to-M, with the benchmarks, S-to-S/M-to-M. Finally, we analyse the results and investigate the mechanism of S-to-M mode via the compressed code’s visualization.

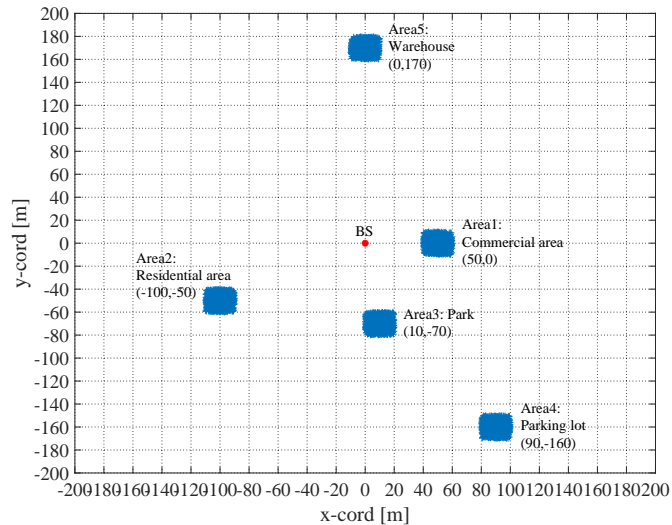


Fig. 7. Locations of the BS and UEs during the channel generation using QuaDRiGa software. UE's position is colored by blue and BS's position by red. Sampling sub-area with the size of $20\text{m} \times 20\text{m}$ is selected in a $400\text{m} \times 400\text{m}$ urban micro cell, where the BS is located in the center (0,0) and UE is randomly located in the sub-area centered on the marked coordinates.

TABLE III

BASIC PARAMETER SETTING IN THE CHANNEL GENERATION USING QUADRIGA SOFTWARE.

Antenna setting	32 ULA antennas at BS single antenna at UE
Operating system	FDD-OFDM system with 512 subcarriers
Center frequency	2.655GHz
Bandwidth	10MHz
Scenarios	3GPP-38.901-UMi-NLOS 3GPP-38.901-UMi-LOS
Space correlation distant	20m
Scattering clusters number	5/10/40
Cell range	$400\text{m} \times 400\text{m}$
Sub-area range	$20\text{m} \times 20\text{m}$
Sampling number in each sub-area	50,000
Sub-area's number/Tasks number	5
CSI Pretreatment	2D-DFT sparse clipping(reserve nonzero 32 rows) normalized to real values in the range [0, 1]

A. CSI Simulation Setting

1) *QuaDRiGa simulation datasets*: The multi-scenarios CSI dataset is simulated by a quasi deterministic radio channel model, QuaDRiGa [24]⁷, which enables the modeling of MIMO radio channels for various specific network configurations and has become popular in academia. Table III shows some basic information in the CSI simulation. We restrict the sub-area's range not over the spatial correlation distance to ensure that the CSI sampled within one sub-area can keep their WSS properties in LSPs.

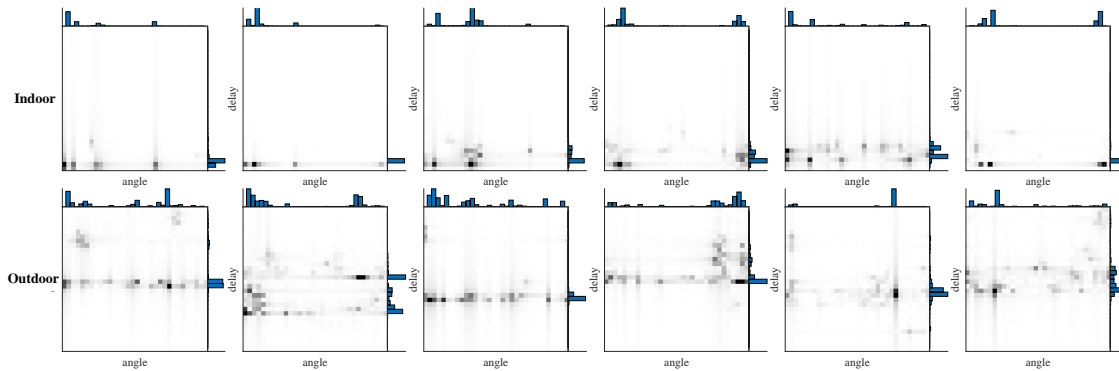
We simulate five typical environments in an urban cell and 7. The scenario setting is given in Table IV, whereas the rest follows the default set according to [24]. Fig2 displays the visualization of the CSI maps. The number of scattering clusters around UE describes the complexity of the environment. The grayscale CSI images show that the rich scattering environments, e.g. commercial area (sub-area1) and residential area (sub-area2), would be reflected in a dense and complex CSI with a wide angular range and delay range, while the CSI map of open scattering environments, park (sub-area3) and parking lot (sub-area4), would be sparse and feature centrally distributed. Moreover, CSI sampled in the same sub-area has higher similarity than cross areas, which the sample correlation is depicted in Fig4

2) *COST2100 Indoor/Outdoor datasets*: To further verify the feasibility of our MTL-based mode, we also conduct the experiments on the widely-used CSI dataset generated by the COST2100 channel model with Indoor/Outdoor scenarios. We use the same dataset in [8], where the simulation settings: The BS is positioned at the center of a square area with lengths of 20m and 400m for indoor and outdoor scenarios, respectively, whereas the UEs are randomly positioned in the square area per sample. We also analyze the CSI feature distribution of the COST2100 Indoor/Outdoor datasets. In Fig8(a), one can intuitively observe that the CSI feature distribution of the two datasets differs a lot. Further observation can be found in Fig8(b) that the difference

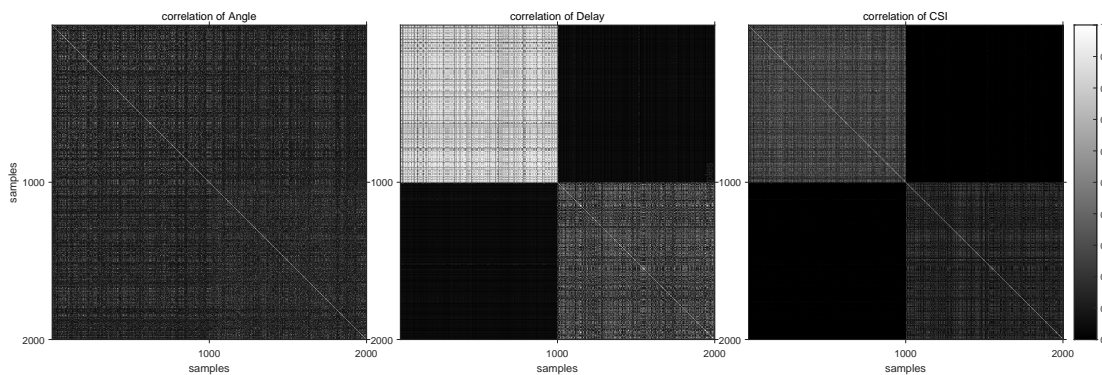
⁷QuaDRiGa simulation software can be download at <https://quadriga-channel-model.de>

TABLE IV
DIFFERENCES IN SIMULATION DATASET BETWEEN SUB-TASKS.

Task	Sub-area	Center position	Scenario	Clusters
task1	Commercial area	(50,0)	3GPP-38.901-UMi-NLOS	40
task2	Residential area	(-100,-50)	3GPP-38.901-UMi-NLOS	40
task3	Park	(10, -70)	3GPP-38.901-UMi-LOS	5
task4	Parking lot	(90, -160)	3GPP-38.901-UMi-LOS	5
task5	Warehouse	(0, 170)	3GPP-38.901-UMi-NLOS	10



(a) Grayscale image of CSI maps in the COST2100 Indoor/Outdoor datasets. The first row contains 6 samples randomly extracted from the Indoor dataset, whereas the samples in second row are from the Outdoor dataset.



(b) Visualizes the sample correlation matrix of PAS/PDP/CSI in the COST2100 Indoor/Outdoor datasets. The first 1000 samples were randomly taken from Indoor dataset, and the last 1000 samples were taken from Outdoor dataset.

Fig. 8. Visualization the differences of the COST2100 Indoor/Outdoor datasets, including the grayscale images and correlation matrix.

of feature distribution mainly comes from the large difference of delay distribution between the two datasets, which the distance between UE and BS is within a range of 20m in the Indoor scenario, whereas the range enlarges to 200m in the Outdoor scenario. In addition, there is no significant difference in the distribution of angular features, for the sampling area does not involve any azimuth information (BS is centered in the sampling area). The sample correlation of the Indoor dataset is higher than that of the Outdoor dataset, which also explains why the same NN always has better performance on the Indoor dataset than the outdoor dataset.

B. NN architecture and training details

1) *NN architecture of various complexity*: Notice that any NN architecture can be adopted in the three modes, we apply NN with various complexity for comparison and validation. For

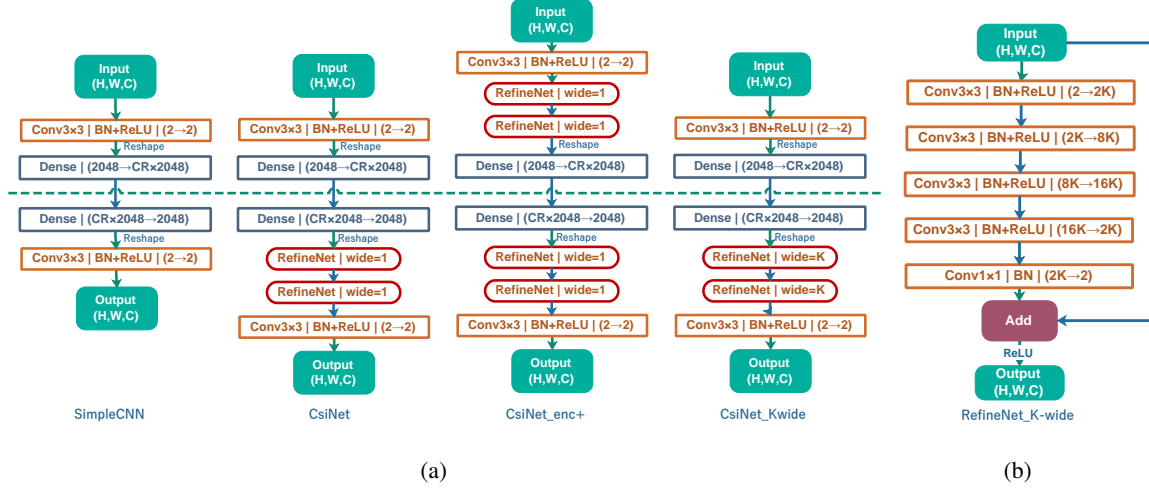


Fig. 9. (a) NN architectures with various complexity involved in the experiment based on CsiNet. (b) RefineNet-K-wide structure. The NN complexity is increased mainly by widening the structure of RefineNet. In each layer, the details are marked as: Type and kernel size | Batch Normalization and ReLU activation | Input channels→Output channels.

convenience, we simply modify the NN’s architecture based on CsiNet [8], depicted in Fig9(a). The NN complexity is increased mainly by widening the structure of RefineNet (CsiNet- K wide) or add additional RefineNet blocks in the encoder NN (CsiNet-enc+). The time and space complexity of the involved NNs is measured by the amount of FLOPs and parameters in Table V.

2) *Training details*: When training with the QuADriGa simulation datasets, each subtask has 50,000 samples, among which training data, validation data and test data account for 85%, 10% and 5% respectively. When training with the COST2100 dataset, the training, validation, and testing sets contain 100,000, 30,000, and 20,000 samples in both indoor and outdoor scenario

TABLE V
TIME AND SPACE COMPLEXITY OF THE INVOLVED NNs

	CR	SimpleCNN	CsiNet	CsiNet-enc+	CsiNet-8wide	CsiNet-16wide
FLOPs(AE)[M]	1/4	2.17	6.23	10.30	210.44	833.95
	1/8	1.12	5.19	9.25	209.40	832.91
	1/16	0.60	4.66	8.72	208.87	832.38
	1/32	0.34	4.40	8.46	208.61	832.12
	1/64	0.20	4.27	8.33	208.48	831.99
Para(AE)[M]	1/4	2.10	2.10	2.11	2.30	2.91
	1/8	1.05	1.05	1.06	1.25	1.86
	1/16	0.53	0.53	0.53	0.73	1.34
	1/32	0.27	0.27	0.27	0.47	1.08
	1/64	0.14	0.14	0.14	0.34	0.95

datasets, respectively. We use the training optimizer Adam and the learning rate is set as $1e-3$. The training epoch is 1200, and early stopping method is adopted to avoid the overfitting problem.

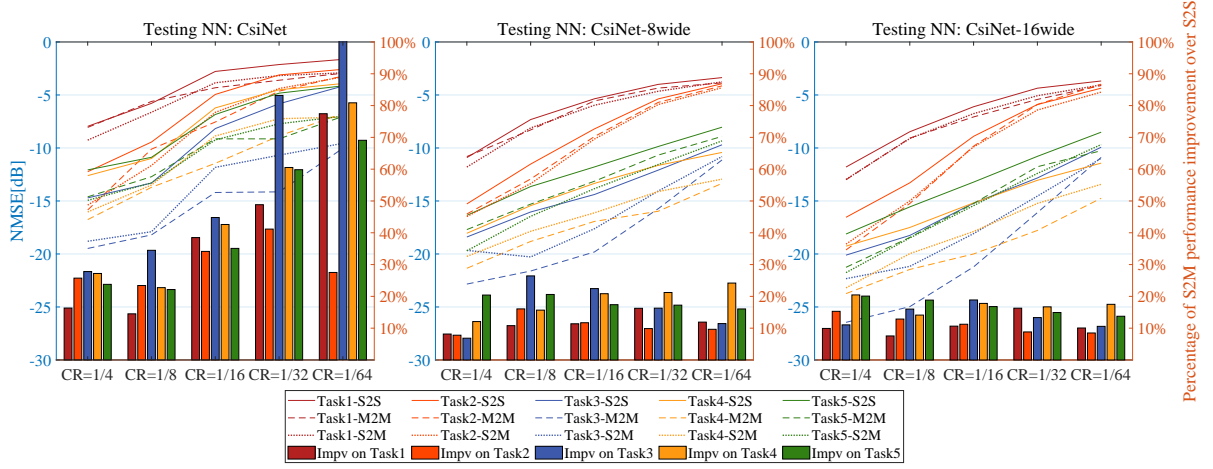
The supervised learning of the GateNet is conducted after the AE's training. We first generated the corresponding one-hot label according to the task category, then pair them with the encoder's output and mix up all the paired samples, i.e. 250,000 QuaDRiGa samples and 200,000 COST2100 samples. The proportion of training, verification and test data is 85%, 10% and 5% respectively. We also use Adam with a learning rate of $1e-3$ and train 200 epochs for all of the experiments.

C. Performance of MTL-based CSI feedback mode

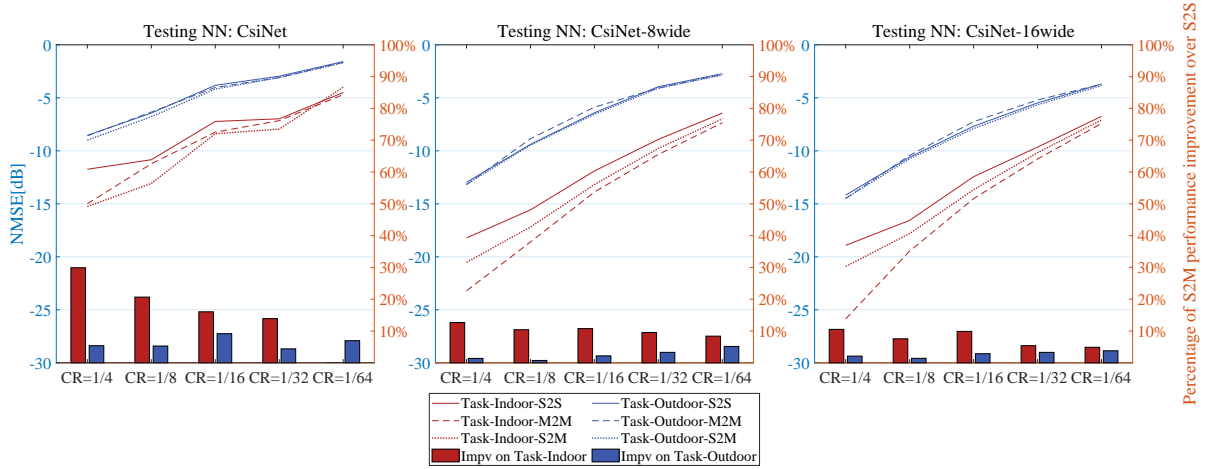
In this subsection, we evaluate and compare the proposed MTL-based CSI feedback deployment mode, S-to-M, with the benchmarks, S-to-S/M-to-M.

1) *Performance of the GateNet:* We first discuss the great performance on the supervised learning of the GateNet: The model converges rapidly to a high accuracy, about 99.95% at 50 epochs. Even with an extreme low CR($CR=1/64$), the accuracy can still converge to 99.85%, which brings negligible effects to our M-to-M mode (The NMSE gap between S-to-M with/without the GateNet is less than $1e-5$). The result manifests that the compressed code has enough valuable information for the classifier to identify its task category.

2) *The feasibility of S-to-M mode:* We conducted the experiences both on the QuaDRiGa simulation datasets and COST2100 Indoor/Outdoor datasets, where the results depicted in Fig10 can manifest the feasibility of our MTL-based mode. Several conclusions can be summarized as follows: (a) For a same NN structure, the short-dotted line S-to-M and long-dotted line M-to-M are much below the solid line S-to-S, indicating that the multitasking modes, S-to-M and M-to-M, perform better than S-to-S due to the effect of decomposing a challenging task into several relatively easy sub-tasks. This observation can also be found in the positive bar values (percentage of S-to-M performance improvement over S-to-S). (b) As for multitasking modes, S-to-M can achieve performance equal to (or even better than) M-to-M with fewer sets of encoder's parameters as well as avoiding switching encoder's NN parameters when the UE moves across sub-areas. This beneficial comes from the hard sharing mechanism of MTL that the shared encoder can access to all the sub-task's samples, which can be regard as a kind of data enhancement effect, resulting a reduction of the model overfitting risk. Thus, perhaps a



(a) Training on the QuaDRiGa simulation datasets



(b) Training on the COST2100 Indoor/Outdoor datasets

Fig. 10. Performance of S-to-S/M-to-M/S-to-M mode of various NN and CR trained on the QuaDRiGa simulation datasets (a) or the COST2100 Indoor/Outdoor datasets (b). We tests 3 NNs of different complexity increasing from left to right. In each subgraph, the X axis represents CR, the line depicts the NMSE performance corresponding to the left Y axis, while the bar depicts the percentage of S-to-M performance improvement over S-to-S corresponding to the right Y axis. All the 5 sub-tasks are color-coded, and the S-to-S/M-to-M/S-to-M modes are presented with solid, long-dotted and short-dotted line, respectively.

shared encoder with smaller capacity can achieve the same or better generalization capability than a more complex encoder.

Other secondary observations on the differences in performance for different subtasks, CR or NN complexity are following depicted: The performance improvement of S-to-M over than S-to-S is enlarged when applying an easier NN; the NMSE gap between S-to-M/M-to-M and S-to-S is larger in easy subtask(e.g. QuaDRiGa subtask3 or COST2100 task-Indoor) than in hard one(e.g.

QuaDRiGa subtask1 or COST2100 task-Outdoor). For the network with high complexity, the multitasking modes may become less profitable, because the sub-task's data samples are not enough to support the training of a too complex network, which may lead to over-fitting. This problem can be solved by preparing adequate training data or data enhancing.

The experimental results on COST21000 are consistent with those on QuaDRiGa dataset, except that in the Outdoor subtask, the multitasking modes show no obvious advantage over S-to-S, as the NMSE performance lines of the three modes are almost overlapping, and the performance improvement ratio (blue bar) is also very low. This phenomenon can be explained from the perspective of transfer learning. For the Indoor-task, the small sampling range and the high sample similarity guarantee an easy-handled sub-task, where 100,000 training samples are enough for NN to grasp the feature representation. Yet mixed training with other samples with large differences will only bring performance loss of network in the current task, i.e. Outdoor samples bring much negative transfer effect to the Indoor-task. In this situation, M-to-M is a better selection for the Indoor-task than S-to-S, and then the MTL-based improved version, S-to-M, can be adopted for the sake of UE's convenience. While for the Outdoor-task, the sampling range enlarges to 100 times of the Indoor-task and 100,000 samples are far less enough for training, which explains why NN always obtains worse performance than on the Indoor-task. Due to the large differences between the Indoor/Outdoor samples, adding additional Indoor samples could hardly bring any valuable assistant for NN to fit the feature distribution of the Outdoor samples, thus the performances of the three modes on the Outdoor task are almost identical. To avoid formidable tasks like the Outdoor-task, we can appropriately narrow the sampling range to improve the sample similarity, i.e. further segment the 200m×200m Outdoor sampling place and decompose this complex task into several easy-handling sub-tasks, where our S-to-M mode can bring noticeable performance enhancement.

3) *The advantages of S-to-M mode:* As mentioned above, when facing with a large CSI sampling cell, two modes are usually adopted:

- S-to-S mode with a rather complex NN to handle the CSI in the global cell.
- M-to-M mode with multiple relatively simple NNs, each handles the feedback of CSI in a local sub-area.

we describe the advantages of S-to-M mode by comparing with the above two modes in Fig11 and TabVI, respectively.

Fig11 shows the trade off between NN complexity and performance, where we can compare the

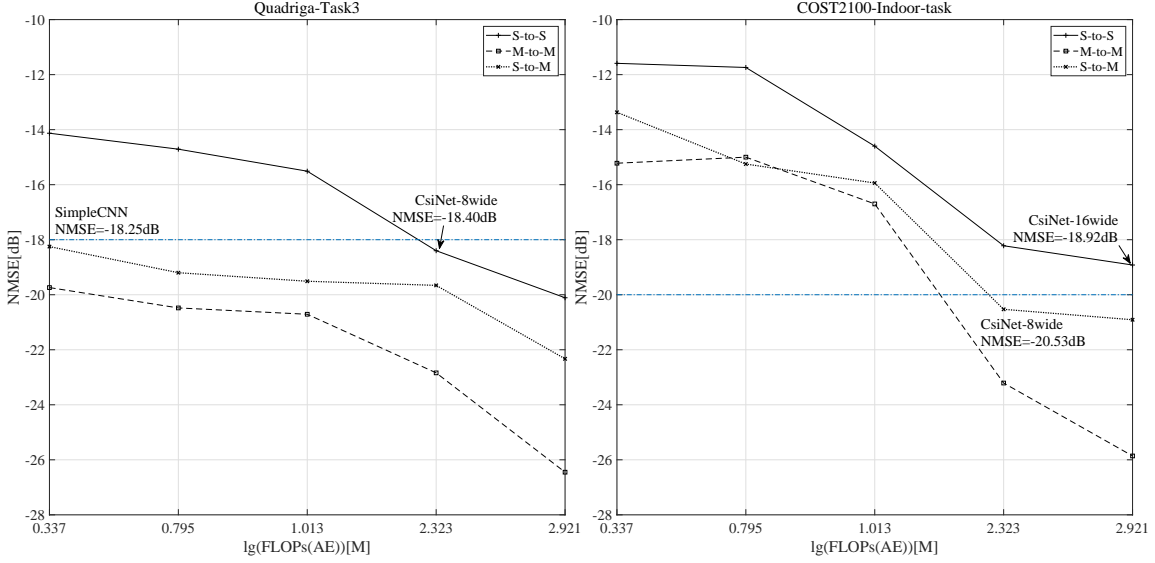


Fig. 11. Model Complexity VS Performance in S-to-S/S-to-M/M-to-M mode on the QuaDRiGa-Task3 (left) or the COST2100-Indoor-task (right) when $CR=1/4$. The x axis stands for the NN's time complexity, represented by $\lg(\text{FLOPs}(\text{AE}))$ in millions, and Y axis stands for the NMSE performance. The three modes are distinguished with different line-style and some special data points are highlighted in the diagram.

NN complexity of S-to-M and S-to-S when they obtain a same level of NMSE performance. We simply chose the experiment result on the QuaDRiGa Task3 (left sub-graph) and the COST2100 Indoor-task (right sub-graph) as two examples for illustration. Models on the blue horizontal line, $\text{NMSE}=-18\text{dB}$ in the left and $\text{NMSE}=-20\text{dB}$ in the right, achieve similar performance. In the QuaDRiGa Task3's result (left), to achieve similar performance with S-to-M, S-to-S needs to increase the FLOP of NN from SimpleCNN's 2.17M to Csinet-8wide's 210.44M, nearly 100 times. In the COST2100 Indoor-task result (right), S-to-M obtains better NMSE performance than -20dB with a 210.44M FLOPs NN, while S-to-S's performance cannot reach -20dB even with a more complex 833.95M FLOPs NN. From the experimental result, we observe that to obtain the same level of NMSE performance, the NN structure of S-to-S is far more complex than that of S-to-M, even $\text{FLOPs}(S-to-S)$ is much more than $T \times \text{FLOPs}(S-to-M)$, where T is the sub-task number.

S-to-M outperforms S-to-S on both datasets, suggesting that for the first case (learning the global cell's CSI with a complex S-to-S network), this deployment mode yields lower benefits than the region-specific S-to-M mode proposed in this paper. On the one hand, for the same

level of reconstruction accuracy, S-to-M can greatly reduce the complexity of the network. On the other hand, the reconstruction accuracy obtained by S-to-M is also higher under the same network complexity.

As for comparing with the second case of applying multiple region-specific and relatively simple NNs in the M-to-M mode, we demonstrate the merits of S-to-M that the encoder memory consumption is much reduced yet with negligible performance loss. Table VI shows the NMSE [dB] performance of CsiNet on the QuaDriGa or the COST2100 dataset, where the best are marked in bold. Due to the MTL-based hard sharing mechanism, S-to-M can shrink encoder memory consumption to $1/T$ of M-to-M and still achieve performance as good as M-to-M. In addition, with the classifier GateNet deployed at the BS, the S-to-M mode can completely eliminate the link of following the region switching network in the M-to-M mode, which not only realizes the UE-friendly design, but also avoids the delay in the M-to-M mode caused by the feedback of additional environmental information from the UE to the BS.

4) *Interpretability of the shared encoder's mechanism in S-to-M*: In the structure of an Auto-Encoder, the encoder works as a compressor to obtain an efficient data representation of the input CSI matrix, and its performance is measured by the accuracy of the decoder's reconstruction of the compressed coding. The encoder of S-to-M performs much better than S-to-S, even though both are accessible to all the sub-tasks data via the same encoder NN structure. Considering

TABLE VI
NMSE PERFORMANCE OF CSINET ON TWO DATASETS

CR	Mode	QuaDRiGa					Cost2100	
		Task1	Task2	Task3	Task4	Task5	Indoor	Outdoor
1/4	S-to-S	-7.96	-12.24	-14.71	-12.61	-12.07	-11.74	-8.54
	M-to-M	-8.06	-15.85	-19.48	-16.76	-14.61	-15.00	-8.59
	S-to-M	-9.26	-15.39	-18.80	-16.04	-14.94	-15.25	-9.00
1/8	S-to-S	-5.79	-9.44	-13.31	-10.99	-10.88	-10.84	-6.44
	M-to-M	-5.61	-10.11	-18.20	-13.71	-12.71	-11.22	-6.34
	S-to-M	-6.63	-11.65	-17.90	-13.49	-13.29	-13.08	-6.78
1/16	S-to-S	-2.78	-4.95	-8.17	-6.22	-6.84	-7.23	-3.82
	M-to-M	-4.32	-7.55	-14.20	-11.45	-9.14	-8.24	-4.02
	S-to-M	-3.85	-6.64	-11.83	-8.87	-9.24	-8.39	-4.17
1/32	S-to-S	-2.13	-3.11	-5.83	-4.51	-4.83	-6.98	-2.96
	M-to-M	-3.61	-4.64	-14.14	-8.87	-9.14	-7.15	-3.09
	S-to-M	-3.17	-4.39	-10.68	-7.24	-7.72	-7.95	-3.09
1/64	S-to-S	-2.64	-2.98	-8.16	-5.92	-6.14	-4.50	-1.58
	M-to-M	-2.95	-3.21	-10.03	-6.74	-7.02	-4.70	-1.65
	S-to-M	-2.91	-3.29	-9.56	-7.09	-7.00	-4.00	-1.69

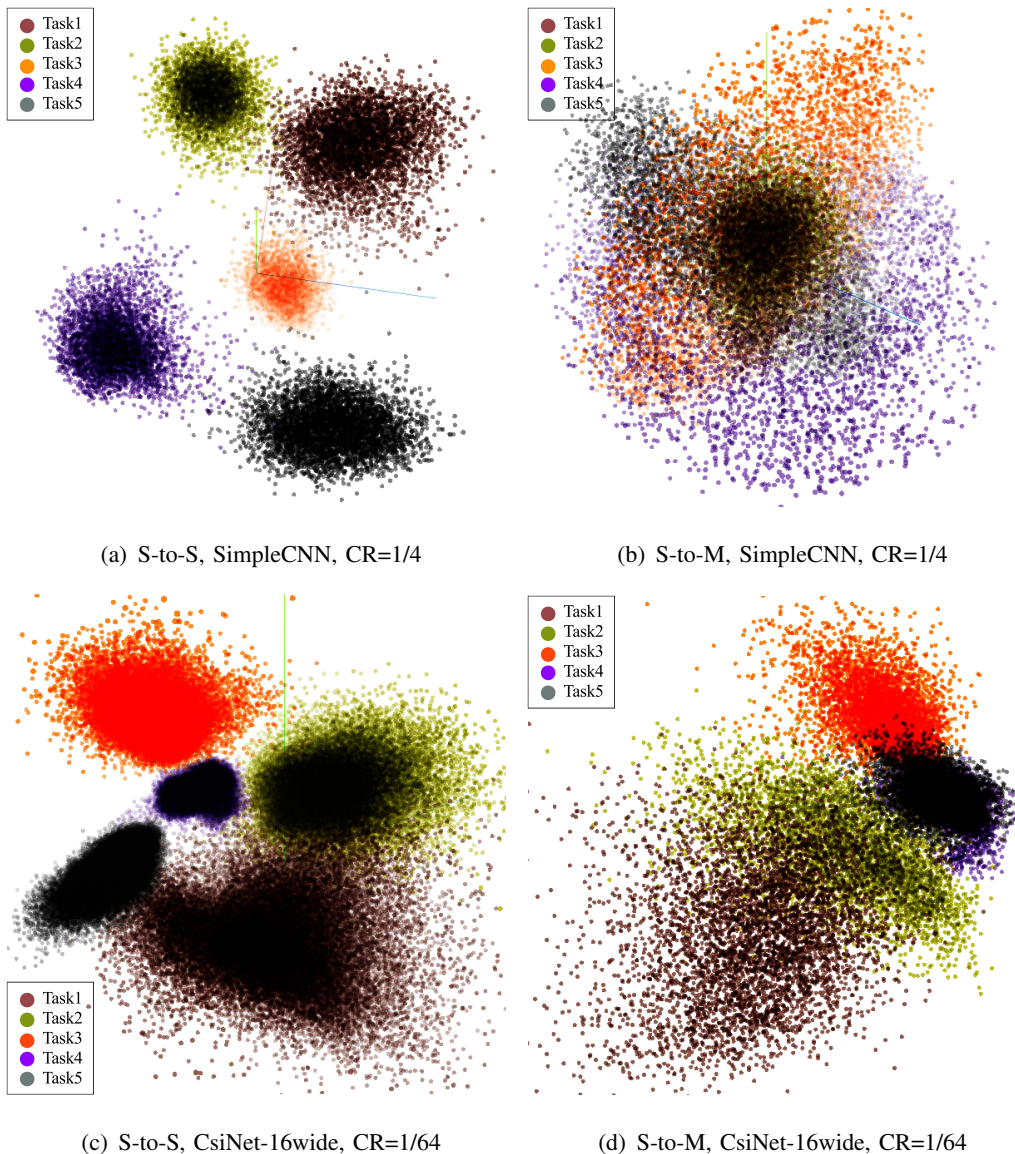


Fig. 12. Visualization of the encoder’s output in the S-to-S or S-to-M mode on QuaDRiGa-5-subtasks dataset. The potential space is $K = CR \times 2048$ dimensional (512-dimensional SimpleCNN in the first row, 32-dimensional CsiNet-16wide in the second row). The first and second column show the compression code feature distribution of the S-to-S and S-to-M, respectively. Principal Component Analysis(PCA) is adopted here to further map the K -length vectors into 2-dimensional ones for visualization. 10,000 random -selective samples in each subtask are depicted in each graph, and all the 5 sub-tasks are color-coded.

this observation, we further investigate the mechanism of S-to-M mode from the perspective of AE’s unsupervised learning via the compressed code’s visualization.

Specifically, in the process of mapping the high-dimensional CSI data to the representation vector of the low-dimensional embedding space, a good encoder can make the distribution of sample points in the potential embedding space sufficiently dispersed and the difference of

sample points sufficiently obvious. Only in this way can the decoder distinguish the difference between samples during reconstruction. Otherwise, if two disparate CSI samples are encoded into two overlapping embedding points, the decoder may reconstruct them into very similar or even identical matrix, for the decoder can be viewed as a generator to generate the original high dimensional CSI only from the information contained in the embedding vectors.

Fig12 displays the visualization of the embedding vector in the S-to-S or S-to-M mode on QuaDRiGa-5-subtasks dataset. To intuitively observe the characteristics of data distribution, we apply the Principal Component Analysis (PCA), a widely used linear data dimension reduction method in the visual analysis domain, to further map the $K = CR \times 2048$ -length vectors into the 2-dimensional plane for visualization. Each subtask contains 10,000 samples in the plain. In the left column, S-to-S encoder's output, the encoder has to distribute the samples of all subtasks dispersively in the K -dimensional embedding space, where storing all 50,000 scatter points may become too crowded to manage. In contrast to S-to-S, the S-to-M embedding space is looser because samples of intersecting subtasks are allowed to overlap when mapped to the representation embedding space. Since the shared encoder corresponds to multiple task-specific and independent decoders, it creates multiple paralleled, separate, non-interfering embedding spaces for the compressed code, each corresponding to a task-specific decoder. The above analysis explains the phenomenon that points of different colors distribute in different areas in Fig12(a)12(c), yet can be overlap or bridged together in Fig12(b)12(d). We can also view the S-to-M's embedding space as five paralleled spaces overlap together, each only containing the corresponding subtask's samples. Due to the multifold expansion of the representation space, the shared encoder is easier to process and accommodate sample points to be sufficiently dispersed in the representation space, i.e. the ability of the shared encoder to represent features is improved by this hard-sharing mechanism.

Moreover, we demonstrate the rationality of S-to-M's superiority over S-to-S from the perspective of unsupervised learning in AE [37]. In the S-to-S's unsupervised learning, the result in Fig12(a)12(c) displays an obvious clustering process. The encoder takes a lot of energy to learn the difference of sample distribution patterns between different subtasks (crossing categories), resulting in insufficient attention to the sample difference of the same subtask (within the category). However, S-to-M chooses semi-supervised learning, an organic combination of unsupervised and supervised learning: the samples are manually classified by regional labels, which eliminates the clustering process of S-to-S. Thus the encoder pays more attention to the

sample differences within the category in the regression task. At the same time, the GateNet's supervised learning classification is applied to extract the feature distribution differences across categories.

V. CONCLUSION

For the deployment mode of CSI feedback DL-based methods, we prefer the multitasking manner of dividing the CSI dataset of multiple scenarios by region and feedback by region. Based on this, we propose the S-to-M mode with GateNet of the MTL-based framework, i.e. a shared encoder corresponds to multiple task-specific decoders and a classifier to identify the task number from the encoder's output. S-to-M is designed to save the consumption of UE's computing power or storage capacity, making up the shortages in S-to-S or M-to-M mode: (1) Compared with S-to-S, S-to-M much reduces the NN complexity via decomposing the challenging task into several relatively easy sub-tasks; (2) S-to-M improves M-to-M via applying MTL and lets the UE only save one set encoder's parameters, much saving UE's memory consumption. Moreover, GateNet is designed to address the problem of adding additional feedback overhead or procedure when switching networks, which realizes the UE-friendly design as well as improves the communication system's efficiency.

In the future work, the proposed MTL-based CSI feedback deployment mode will be further extended to a concept of electronic map, which can be regarded as a kind of environmental Knowledge Base (KB). Each sub-area within the global cell should be marked with electronic map label based on its own environmental scattering characteristic. The framework of S-to-M mode can hence provide the electronic map for BS to preload when being first deployed in the cell, where the environmental KB is contained in the multiple task-specific decoders. More Efficient and intelligent environmental electronic map design will be in the future work, which may involves various factors, e.g. task correlation or resource allocation, and dynamic self-adaptive and self-tuning optimization is also demanded due to the variations of the environment overtime.

REFERENCES

- [1] N. Alliance, "5G white paper," *Next generation mobile networks, white paper*, vol. 1, no. 2015, 2015.
- [2] Q. Bi, "Ten trends in the cellular industry and an outlook on 6G," *IEEE Commun. Mag.*, vol. 57, no. 12, pp. 31–36, Dec. 2019.

- [3] F. Tariq, M. R. A. Khandaker, K. Wong, M. A. Imran, M. Bennis, and M. Debbah, "A speculative study on 6G," *IEEE Wireless Commun.*, vol. 27, no. 4, pp. 118–125, Aug. 2020.
- [4] T. L. Marzetta, "Noncooperative cellular wireless with unlimited numbers of base station antennas," *IEEE Trans. Wireless Commun.*, vol. 9, no. 11, pp. 3590–3600, Nov. 2010.
- [5] L. Lu, G. Y. Li, A. L. Swindlehurst, A. Ashikhmin, and R. Zhang, "An overview of massive MIMO: Benefits and challenges," *IEEE J. Sel. Topics Signal Process.*, vol. 8, no. 5, pp. 742–758, Oct. 2014.
- [6] D. J. Love, R. W. Heath, V. K. N. Lau, D. Gesbert, B. D. Rao, and M. Andrews, "An overview of limited feedback in wireless communication systems," *IEEE J. Sel. Areas Commun.*, vol. 26, no. 8, pp. 1341–1365, Oct. 2008.
- [7] P.-H. Kuo, H. Kung, and P.-A. Ting, "Compressive sensing based channel feedback protocols for spatially-correlated massive antenna arrays," in *2012 IEEE Wireless Communications and Networking Conference (WCNC)*. IEEE, 2012, pp. 492–497.
- [8] C. Wen, W. Shih, and S. Jin, "Deep learning for massive MIMO CSI feedback," *IEEE Wireless Commun. Lett.*, vol. 7, no. 5, pp. 748–751, Oct. 2018.
- [9] J. Schmidhuber, "Deep learning in neural networks: An overview," *Neural networks*, vol. 61, pp. 85–117, Jan. 2015.
- [10] T. Wang, C.-K. Wen, H. Wang, F. Gao, T. Jiang, and S. Jin, "Deep learning for wireless physical layer: Opportunities and challenges," *China Communications*, vol. 14, no. 11, pp. 92–111, 2017.
- [11] Z. Qin, H. Ye, G. Y. Li, and B.-H. F. Juang, "Deep learning in physical layer communications," *IEEE Wireless Communications*, vol. 26, no. 2, pp. 93–99, 2019.
- [12] P. Baldi, "Autoencoders, unsupervised learning, and deep architectures," in *Proceedings of ICML Workshop on Unsupervised and Transfer Learning*, ser. Proceedings of Machine Learning Research, I. Guyon, G. Dror, V. Lemaire, G. Taylor, and D. Silver, Eds., vol. 27. Bellevue, Washington, USA: PMLR, 02 Jul 2012, pp. 37–49. [Online]. Available: <https://proceedings.mlr.press/v27/baldi12a.html>
- [13] Z. Lu, J. Wang, and J. Song, "Multi-resolution csi feedback with deep learning in massive mimo system," in *ICC 2020-2020 IEEE International Conference on Communications (ICC)*. IEEE, 2020, pp. 1–6.
- [14] Z. Cao, W.-T. Shih, J. Guo, C.-K. Wen, and S. Jin, "Lightweight convolutional neural networks for CSI feedback in massive MIMO," *IEEE Commun. Lett.*, 2021, Early access.
- [15] B. Tolba, M. Elsabrouty, M. G. Abdu-Aguye, H. Gacanin, and H. M. Kassem, "Massive mimo csi feedback based on generative adversarial network," *IEEE Communications Letters*, vol. PP, no. 99, pp. 1–1, 2020.
- [16] J. Guo, C.-K. Wen, S. Jin, and G. Y. Li, "Convolutional neural network-based multiple-rate compressive sensing for massive mimo csi feedback: Design, simulation, and analysis," *IEEE Transactions on Wireless Communications*, vol. 19, no. 4, pp. 2827–2840, 2020.
- [17] J. Yang, X. Chen, H. Zou, D. Wang, Q. Xu, and L. Xie, "Efficientfi: Towards large-scale lightweight wifi sensing via csi compression," *IEEE Internet of Things Journal*, pp. 1–1, 2021.
- [18] T. Wang, C. K. Wen, S. Jin, and G. Y. Li, "Deep learning-based csi feedback approach for time-varying massive mimo channels," *IEEE Wireless Communications Letters*, pp. 1–1, 2018.
- [19] J. Guo, C.-K. Wen, and S. Jin, "CANet: Uplink-aided downlink channel acquisition in fdd massive mimo using deep learning," *IEEE Transactions on Communications*, vol. 70, no. 1, pp. 199–214, 2022.
- [20] J. Guo, Y. Zuo, C.-K. Wen, and S. Jin, "User-centric online gossip training for autoencoder-based CSI feedback," *IEEE J. Sel. Topics Signal Process.*, 2022, Early access.
- [21] J. Poutanen, K. Haneda, L. Liu, C. Oestges, F. Tufvesson, and P. Vainikainen, "Parameterization of the cost 2100 mimo channel model in indoor scenarios," in *European Conference on Antennas & Propagation*, 2011.

- [22] J. Guo, X. Li, M. Chen, P. Jiang, T. Yang, W. Duan, H. Wang, S. Jin, and Q. Yu, "Ai enabled wireless communications with real channel measurements: Channel feedback," *Journal of Communications and Information Networks*, vol. 5, no. 3, pp. 310–317, 2020.
- [23] H. Xiao, Z. Wang, W. Tian, X. Liu, W. Liu, S. Jin, J. Shen, Z. Zhang, and N. Yang, "Ai enlightens wireless communication: Analyses, solutions and opportunities on csi feedback," *arXiv preprint arXiv:2106.06759*, 2021.
- [24] S. Jaeckel, L. Raschkowski, K. Börner, and L. Thiele, "QuaDRiGa: A 3-D multi-cell channel model with time evolution for enabling virtual field trials," *IEEE Trans. Antennas Propag.*, vol. 62, no. 6, pp. 3242–3256, 2014.
- [25] T. Evgeniou and M. Pontil, "Regularized multi-task learning," in *Proceedings of the tenth ACM SIGKDD international conference on Knowledge discovery and data mining*, 2004, pp. 109–117.
- [26] R. Hu, L. Jiang, and P. Li, "Hybrid beamforming with deep learning for large-scale antenna arrays," *IEEE Access*, vol. 9, pp. 54 690–54 699, 2021.
- [27] Y. Yang, F. Gao, Z. Zhong, B. Ai, and A. Alkhateeb, "Deep transfer learning-based downlink channel prediction for fdd massive mimo systems," *IEEE Transactions on Communications*, vol. 68, no. 12, pp. 7485–7497, 2020.
- [28] H. Xie, F. Gao, S. Jin, J. Fang, and Y.-C. Liang, "Channel estimation for tdd/fdd massive mimo systems with channel covariance computing," *IEEE Transactions on Wireless Communications*, vol. 17, no. 6, pp. 4206–4218, 2018.
- [29] D. Tse and P. Viswanath, *Fundamentals of wireless communication*. Cambridge university press, 2005.
- [30] K. Pedersen, P. Mogensen, and B. Fleury, "A stochastic model of the temporal and azimuthal dispersion seen at the base station in outdoor propagation environments," *IEEE Transactions on Vehicular Technology*, vol. 49, no. 2, pp. 437–447, 2000.
- [31] O. E. Ayach, S. Rajagopal, S. Abu-Surra, Z. Pi, and R. Jr, "Spatially sparse precoding in millimeter wave mimo systems," *IEEE Transactions on Wireless Communications*, vol. 13, no. 3, pp. 1499–1513, 2013.
- [32] A. Alkhateeb, O. E. Ayach, G. Leus, and R. W. Heath, "Channel estimation and hybrid precoding for millimeter wave cellular systems," *IEEE Journal of Selected Topics in Signal Processing*, vol. 8, no. 5, pp. 831–846, 2017.
- [33] S. Ruder, "An overview of multi-task learning in deep neural networks," *arXiv preprint arXiv:1706.05098*, 2017.
- [34] R. Collobert and J. Weston, "A unified architecture for natural language processing: Deep neural networks with multitask learning," in *Proceedings of the 25th international conference on Machine learning*, 2008, pp. 160–167.
- [35] I. Misra, A. Shrivastava, A. Gupta, and M. Hebert, "Cross-stitch networks for multi-task learning," in *Proceedings of the IEEE conference on computer vision and pattern recognition*, 2016, pp. 3994–4003.
- [36] J. Baxter, "A bayesian/information theoretic model of learning to learn via multiple task sampling," *Machine learning*, vol. 28, no. 1, pp. 7–39, 1997.
- [37] S. Wang, J. Cai, Q. Lin, and W. Guo, "An overview of unsupervised deep feature representation for text categorization," *IEEE Transactions on Computational Social Systems*, vol. 6, no. 3, pp. 504–517, 2019.